

Polytechnic Institute of New York



LEVEL II

MICROWAVE RESEARCH INSTITUTE

POLY-MRI-1407-80
May 1979

AD A 096469

FEED REGION MODES IN DIPOLE PHASED ARRAYS

by

A. Hessel and E. Mayer

DBG FILE COPY.

DISTRIBUTION STATEMENT A

Approved for public release;
Distribution Unlimited

Prepared for

**BALLISTIC MISSILE DEFENSE ADVANCED TECHNOLOGY CENTER
DASG60-76-C-0008**

**DTIC
ELECTE**
MAR 17 1981
S D
D

81 3 16 149

UNCLASSIFIED

SECURITY CLASSIFICATION OF THIS PAGE (When Data Entered)

REPORT DOCUMENTATION PAGE		READ INSTRUCTIONS BEFORE COMPLETING FORM
1. REPORT NUMBER	2. GOVT ACCESSION NO.	3. RECIPIENT'S CATALOG NUMBER
	AD-A096469	
4. TITLE (and Subtitle)		5. TYPE OF REPORT & PERIOD COVERED
6 Feed Region Modes in Dipole Phased Arrays.		9 Technical rept.
		6. PERFORMING ORG. REPORT NUMBER
		14 POLY-MRI-1487-881
7. AUTHOR(s)		8. CONTRACT OR GRANT NUMBER(s)
10 A. Hessel and E. Mayer		
9. PERFORMING ORGANIZATION NAME AND ADDRESS		10. PROGRAM ELEMENT, PROJECT, TASK AREA & WORK UNIT NUMBERS
Polytechnic Institute of New York Microwave Research Institute Route 110, Farmingdale, New York 11735		
11. CONTROLLING OFFICE NAME AND ADDRESS		12. REPORT DATE
Ballistic Missile Defense Advanced Technology Center P.O. Box 1500, Huntsville, Ala. 35807		11 May 1979
14. MONITORING AGENCY NAME & ADDRESS (if different from Controlling Office)		13. NUMBER OF PAGES
12 43		42
		15. SECURITY CLASS. (of this report)
		Unclassified
		15a. DECLASSIFICATION/DOWNGRADING SCHEDULE
16. DISTRIBUTION STATEMENT (of this Report)		
Approved for public release; distribution unlimited.		
17. DISTRIBUTION STATEMENT (of the abstract entered in Block 20, if different from Report)		
18. SUPPLEMENTARY NOTES		
BMDATC Project Engineer: Fan King (ATC-R)		
19. KEY WORDS (Continue on reverse side if necessary and identify by block number)		
Dipole phased arrays, feed-region modes blindspots.		
20. ABSTRACT (Continue on reverse side if necessary and identify by block number)		
Feed region modes are derived for a class of dipole phased arrays. The dipole and its balun are a linearly polarized version of the PAR antenna element, and are modeled in strip-line geometry. Knowledge of the feed region modes is essential in determining the influence of supports on the element scan performance, and should shed light on the formation of blind-spots in dipole arrays. It is shown that for practical spacings the balanced, strip-line feed structure supports a propagating TM mode, in addition to		

DD FORM 1473
1 JAN 73

UNCLASSIFIED

SECURITY CLASSIFICATION OF THIS PAGE (When Data Entered)

412081 YW

Unclassified

SECURITY CLASSIFICATION OF THIS PAGE(When Data Entered)

two TEM modes. The propagation constant of this mode is scan dependent, and under inappropriate conditions its cut-off occurs before the onset of the grating lobe. Pending further analysis, it is conjectured that this mode cut-off may cause the blind spots which limit the array scan coverage.

UNCLASSIFIED

SECURITY CLASSIFICATION OF THIS PAGE(When Data Entered)

ABSTRACT

Feed region modes are derived for a class of dipole phased arrays. The dipole and its balun are a linearly polarized version of the PAR antenna element, and are modelled in strip-line geometry. Knowledge of the feed region modes is essential in determining the influence of supports on the element scan performance, and should shed light on the formation of blindspots in dipole arrays. It is shown that for practical spacings the balanced, strip-line feed structure supports a propagating TM mode, in addition to two TEM modes. The propagation constant of this mode is scan dependent, and under inappropriate conditions its cut-off occurs before the onset of the grating lobe. Pending further analysis, it is conjectured that this mode cut-off may cause the blind spots which limit the array scan coverage.

Accession For	
NTIS GRA&I	<input checked="" type="checkbox"/>
DTIC TAB	<input type="checkbox"/>
Unannounced	<input type="checkbox"/>
Justification	
By	
Distribution/	
Availability Codes	
Dist	Avail and/or Special
A	

TABLE OF CONTENTS

	ABSTRACT	
I.	INTRODUCTION	1
II.	TM _z MODES OF THE FEED REGION FOR A RECTANGULAR LATTICE	3
III.	TEM MODES OF THE FEED REGION FOR A RECTANGULAR LATTICE	9
IV.	TM _z MODES OF THE FEED REGION FOR A TRIANGULAR LATTICE	13
V.	NUMERICAL ANALYSIS	17
VI.	NUMERICAL RESULTS AND CONCLUSIONS	19
	APPENDIX: TEM MODE ORTHOGONALITY	21
	REFERENCES	26

I. INTRODUCTION

Measured dipole element patterns in a number of phased arrays indicate the appearance of blindspots [1,2]. Analyses which disregard the presence of dipole supports [3,4] do not predict such resonances. In order to understand the cause of these blindspots and how to avoid them it is necessary to determine the dipole element performance with inclusion of the feed. To circumvent the ensuing complication of simultaneously satisfying boundary conditions on the dipole arms and on their supports, it is desirable to first determine the modes of the feed region.[†] These modes individually satisfy the boundary conditions on the supports, as well as the Floquet requirements on the unit cell walls. The analysis of a dipole array scan performance will then be reduced to an evaluation of the discontinuity presented by dipole arms between two different unit cell waveguides (one representing the feed region and the other the air region above the array).

Section II is devoted to the derivation of the dispersion relation and the fields for the TM_2 modes of the feed region of a dipole phased array, in strip-line geometry and with a rectangular lattice. Section III discusses the TEM modes supported in this feed region. Section IV addresses the feed region modes for the case of a triangular array grid. Section V discusses details of the numerical analysis. Section VI considers the numerical results and presents a number of

[†] A similar approach was taken in R. Lewis, A. Hessel, G. Knittel, "Performance of a protruding-dielectric waveguide element in a phased array," IEEE Trans. Antennas Propagat., Vol. AP-20, pp. 712-722, Nov. 1972.

conclusions. The appendix is devoted to the orthogonality of the degenerate, feed region TEM modes.

II. TM_2 MODES OF THE FEED REGION FOR A RECTANGULAR LATTICE

A typical dipole array element is shown in Fig. 1, and a simplified ribbon model of the element is seen in Figure 2.

The feed region part of the unit cell may be regarded as a finite section of the infinitely extended, uniform guiding structure pictured schematically in Figure 3.

The strip width is assumed small compared to the free space wavelength. Therefore, the usual approximation of only longitudinal current is made. This in turn implies that only the TM_2 unit cell modes are affected by the strip loading. Hence, only the TM_2 propagation characteristics and the associated modal field distributions need be determined. The strips are invisible to the TE_2 fields which are, therefore, represented in terms of the usual Floquet unit cell modes.

To determine the TM_2 modes two coupled, linear, homogeneous integral equations are set up. These equations express the Floquet boundary conditions on the unit-cell walls as well as the vanishing of the tangential E field on the conducting strips. They are solved by Galerkin's procedure, resulting in modal fields that exactly satisfy the Floquet condition but only approximately fulfil the requirements on the strips.

To set up the integral equations, the axial component of the electric field is expressed in terms of the Green's Function for an infinite, electric-current, line source located in the unit cell-waveguide, with $e^{j(\omega t - \kappa z)}$ variation and the allowed values of κ being as yet undetermined. Accordingly,

$$E_z(\underline{r}; \kappa, \underline{k}_{to}) = e^{-jkz} \left[\int_{\text{strip 1}} \hat{G}(\underline{\rho}, \underline{\rho}'; \kappa, \underline{k}_{to}) J_1(\underline{\rho}') d\rho' + \int_{\text{strip 2}} \hat{G}(\underline{\rho}, \underline{\rho}'; \kappa, \underline{k}_{to}) J_2(\underline{\rho}') d\rho' \right]. \quad (1)$$

In (1) the strip current densities are $J_{1,2}(\underline{\rho}')$, and the unit cell Green's function is

$$\hat{G}(\underline{\rho}, \underline{\rho}', \kappa, \underline{k}_{to}) = - \frac{(k^2 - \kappa^2)}{2d_y \omega \epsilon_0} \sum_{n=-\infty}^{\infty} \frac{1}{k_{xn}} \hat{\gamma}_n(x, x') e^{-jk_{yn}(y-y')} \quad (2)$$

where $k_{yn} = k_{y0} + \frac{2\pi n}{d_y} \quad (3)$

$$k_{xn} = \sqrt{k^2 - \kappa^2 - k_{yn}^2}, \quad \text{Im } k_{kn} \leq 0 \quad (4)$$

$$\hat{\gamma}_n(x, x') = \frac{e^{-jk_{xn}(x-x')}}{e^{j(k_{xn} - \xi)d_{x-1}}} + \frac{e^{jk_{xn}(x-x')}}{e^{j(k_{xn} + \xi)d_{x-1}}} + e^{-jk_{xn}|x-x'|} \quad (5)$$

$$\eta = k_{y0} = k \sin \theta_0 \sin \phi_0 \quad (6)$$

$$\xi = k \sin \theta_0 \cos \phi_0 \quad (7)$$

$$\underline{k}_{to} = \xi \underline{x}_0 + \eta \underline{y}_0 \quad (8)$$

$$\underline{\rho} = x \underline{x}_0 + y \underline{y}_0, \quad \underline{\rho}' = x' \underline{x}_0 + y' \underline{y}_0 \quad (9)$$

$$\underline{r} = \underline{\rho} + z \underline{z}_0 \quad (10)$$

and ϵ_0 is the free space permittivity.

The angles (θ_0, ϕ_0) denote the usual beam pointing angles of a phased array whose broadside direction is \underline{z}_0 . It should be stressed that $k_{x0}d_x$ is not the steering phase shift along x , which is given by ξd_x ; rather, k_{x0} and the other k_{xn} are propagation constants for E-type modes of a phase-shift-wall parallel-plate waveguide of height d_y . These modes travel in the x -direction and have

$e^{-j(k_{yn}y + \kappa z)}$ transverse variation.

By enforcing the boundary conditions of the strips, i.e.

$$E_z(\mp \frac{w}{2}, 0) = 0 \quad \text{for } |y| \leq \frac{h}{2}, \quad (11)$$

the following coupled integral equations for $J_{1,2}$ are obtained from (1):

$$\hat{G}(-\frac{w}{2}, y, -\frac{w}{2}, y'; \kappa, \underline{k}_{to}) J_1(y') + \hat{G}(-\frac{w}{2}, y, \frac{w}{2}, y'; \kappa, \underline{k}_{to}) J_2(y') = 0$$

$$\text{for } |y| \leq \frac{h}{2} \quad (12)$$

and

$$\hat{G}(\frac{w}{2}, y, -\frac{w}{2}, y'; \kappa, \underline{k}_{to}) J_1(y') + \hat{G}(\frac{w}{2}, y, \frac{w}{2}, y'; \kappa, \underline{k}_{to}) J_2(y') = 0$$

$$\text{where } \hat{G} \equiv \int_{-\frac{h}{2}}^{\frac{h}{2}} \hat{G} J dy' \quad (\text{see Fig. 3}). \quad (13)$$

In general, to solve (12) and (13), the current densities would be expanded in a set of linearly independent basis functions. However, in view of the narrow strip width only one term of the expansion is used here, i.e.,

$$J_{1,2}(y') = \alpha_{1,2}\psi(y'). \quad (14)$$

Application of Galerkin's method now yields the equations

$$\begin{pmatrix} Z_{11}(\kappa, \underline{k}_{to}) & Z_{12}(\kappa, \underline{k}_{to}) \\ Z_{21}(\kappa, \underline{k}_{to}) & Z_{22}(\kappa, \underline{k}_{to}) \end{pmatrix} \begin{pmatrix} \alpha_1 \\ \alpha_2 \end{pmatrix} = 0 \quad (15)$$

$$\text{where } jZ_{pq}(\kappa, \underline{k}_{to}) = \langle \psi(y), \hat{G}((-1)^p(\frac{w}{2}), y, (-1)^q(\frac{w}{2}), y'; \kappa, \underline{k}_{to}) \psi(y') \rangle, \quad (16)$$

$$\text{and } \langle f, g \rangle \equiv \int_{-\frac{h}{2}}^{\frac{h}{2}} fg \, dy \quad (17)$$

(the form jZ_{pq} is introduced so that Z_{11} and Z_{22} are real).

In view of the following symmetries in (5):

$$\hat{y}_n(x', x') = \hat{y}_n(-x', -x') \quad (18)$$

and

$$j \frac{\hat{y}_n(x, x')}{k_{xn}} = \left[\frac{j\hat{y}_n(x', x)}{k_{xn}} \right]^* \quad (19)$$

equations (15) can be written

$$\begin{pmatrix} Z_{11}(\kappa, \underline{k}_{to}) & Z_{12}(\kappa, \underline{k}_{to}) \\ Z_{12}^*(\kappa, \underline{k}_{to}) & Z_{11}(\kappa, \underline{k}_{to}) \end{pmatrix} \begin{pmatrix} \alpha_1 \\ \alpha_2 \end{pmatrix} = 0 \quad (20)$$

For the choice $\psi(y') = 1$, i.e., a constant current distribution on each strip,

$$Z_{11}(\kappa, \underline{k}_{to}) = \sum_{n=-\infty}^{\infty} \frac{1}{k_{xn}} \cdot \frac{\text{sink}_{xn} d_x}{\text{cos}k_{xn} d_x - \text{cos}\xi d_x} \cdot \left(\frac{\sin \frac{k_{yn} h}{2}}{\frac{k_{yn} h}{2}} \right)^2 \quad (21)$$

$$Z_{12}(\kappa, \underline{k}_{to}) = \sum_{n=-\infty}^{\infty} \frac{1}{k_{xn}} \cdot \frac{\sin k_{xn}(d_x - w) + e^{j\xi d_x} \sin k_{xn} w}{\cos k_{xn} d_x - \cos \xi d_x} \cdot \left(\frac{\sin \frac{k_{yn} h}{2}}{\frac{k_{yn} h}{2}} \right)^2 \quad (22)$$

Alternatively, if $\psi(y')$ is chosen to be the static distribution

$$\psi(y') = \frac{1}{\sqrt{\left(\frac{h}{2}\right)^2 - y'^2}} \quad , \quad (23)$$

which satisfies the edge condition on the strip, then the zeroth order Bessel function of first kind $J_0\left(\frac{k_{yn} h}{2}\right)$, replaces $\left(\frac{\sin \frac{k_{yn} h}{2}}{\frac{k_{yn} h}{2}}\right)$ in (21) and (22).

Scan dependent solutions for $\alpha_{1,2}$ exist only for values of κ satisfying

$$Z_{11}^2(\kappa, \underline{k}_{to}) - |Z_{12}(\kappa, \underline{k}_{to})|^2 = 0 \quad , \quad (24)$$

which is the desired dispersion relation. Its solutions yield, to within our approximations, the propagation constants of the TM_2 modes, guided by the two-conductor strip-line in a unit cell. The κ 's depend on frequency, on geometry and, unlike in closed waveguides, on scan variables. It can be shown in the usual manner that the values of κ are either real or purely imaginary.

For a particular κ , the associated $\alpha_{1,2}$ are evaluated from (20) to within a normalization constant, and the relative current distribution on the strips is thus determined. Subsequently, E_z is calculated from (1) and other field components are obtained from Maxwell's equations. The modes so derived are mutually orthogonal, although they only approximately satisfy the boundary conditions on the strips

[5]. It can also be shown that these TM_2 modes are orthogonal to the TE_2 Floquet modes as well as to the TEM modes derived in the next section.

III. TEM MODES OF THE FEED REGION FOR A RECTANGULAR LATTICE

The TEM modal fields cannot be determined in the same manner as the TM fields because now E_z is identically zero. Instead, the electrostatic potentials on the metallic strips are assigned constant values ϕ_1 and ϕ_2 respectively. Two coupled, inhomogeneous, linear, integral equations of the first kind are set up which express this requirement. Application of Galerkin's procedure yields a set of inhomogeneous, linear, algebraic equations which are solved for the charge density η , or the TEM current density J , where $J = \frac{\omega}{k} \eta$. To formulate the integral equations, the static Green's function for an infinite z-directed line charge in a unit cell is employed. The Green's function is given by

$$G(\rho, \rho'; \underline{k}_{to}) = \frac{1}{2d_y \epsilon_0} \sum_{n=-\infty}^{\infty} \frac{1}{k_{yn}} \gamma_n(x, x') e^{-jk_{yn}(y-y')} \quad (25)$$

with

$$\gamma_n(x, x') = \frac{e^{-k_{yn}(x-x')}}{e^{(k_{yn}-j\xi)d_{x-1}}} + \frac{e^{k_{yn}(x-x')}}{e^{(k_{yn}+j\xi)d_{x-1}}} + e^{-k_{yn}|x-x'|} \quad (26)$$

The wavenumbers k_{yn} , ξ and \underline{k}_{to} are defined in (6-8). If the strip charge densities are designated $\eta_1(y')$ and $\eta_2(y')$, respectively, the resulting potential in the unit cell is

$$\begin{aligned} \phi(x, y) = & \int_{\text{strip 1}} G(\rho, \rho'; \underline{k}_{to}) \eta_1(y') dy' \\ & + \int_{\text{strip 2}} G(\rho, \rho'; \underline{k}_{to}) \eta_2(y') dy' \end{aligned} \quad (27)$$

The boundary conditions on the conductors yield the integral equations,

$$\phi_1 = G(-\frac{w}{2}, y, -\frac{w}{2}, y'; \underline{k}_{to})\eta_1(y') + G(-\frac{w}{2}, y, \frac{w}{2}, y'; \underline{k}_{to})\eta_2(y') \quad \text{for } |y| \leq \frac{h}{2} \quad (28)$$

$$\phi_2 = G(\frac{w}{2}, y, -\frac{w}{2}, y'; \underline{k}_{to})\eta_1(y') + G(\frac{w}{2}, y, \frac{w}{2}, y'; \underline{k}_{to})\eta_2(y'),$$

where $G\eta$ is defined as in (13).

Again, assuming a single mode approximation

$$\eta_{1,2}(y') = \alpha_{1,2}\psi(y') \quad (29)$$

and using the symmetries of (26),

$$\gamma_n(x', x') = \gamma_n(-x', x') \quad (30)$$

and

$$\gamma_n(x, x') = \gamma_n^*(x', x) \quad (31)$$

the Galerkin procedure yields

$$\begin{pmatrix} P_{11}(\underline{k}_{to}) & P_{12}(\underline{k}_{to}) \\ P_{12}^*(\underline{k}_{to}) & P_{11}(\underline{k}_{to}) \end{pmatrix} \begin{pmatrix} Q_1 \\ Q_2 \end{pmatrix} = \begin{pmatrix} \phi_1 \\ \phi_2 \end{pmatrix} \quad (32)$$

$$\text{where } \langle \psi(y), 1 \rangle^2 P_{1q}(\underline{k}_{to}) = \langle \psi(y), G(-\frac{w}{2}, y, (-1)^q(\frac{w}{2}), y'; \underline{k}_{to})\psi(y') \rangle \quad (33)$$

and

$$Q_{1,2} = \alpha_{1,2} \langle \psi(y), 1 \rangle \quad (34)$$

are the electric charges per unit length z on the strips.

For $\psi(y') = 1$,

$$P_{11}(\underline{k}_{to}) = -\frac{1}{\epsilon_0} \sum_{n=-\infty}^{\infty} \frac{1}{2d_y k_{yn}} \frac{\sinh k_{yn} \frac{d_x}{2}}{\cos \xi d_x - \cosh k_{yn} \frac{d_x}{2}} \left(\frac{\sin \frac{k_{yn} h}{2}}{\frac{k_{yn} h}{2}} \right)^2 \quad (35)$$

and

$$P_{12}(k_{to}) = -\frac{1}{\epsilon_0} \sum_{n=-\infty}^{\infty} \frac{1}{2d_y k_{yn}} \frac{e^{j\xi d_x} \sinh k_{yn} w + \sinh k_{yn} (d_x - w)}{\cos \xi d_x - \cosh k_{yn} d_x} \left(\frac{\sin \frac{k_{yn} h}{2}}{\frac{k_{yn} h}{2}} \right)^2 \quad (36)$$

In general, matrix \underline{P} in (32) is non-singular and, therefore, one has from (32)

$$\begin{pmatrix} Q_1 \\ Q_2 \end{pmatrix} = \underline{C} \begin{pmatrix} \phi_1 \\ \phi_2 \end{pmatrix}, \quad (37)$$

where the capacitance matrix, \underline{C} , is \underline{P}^{-1} .

Choosing a particular combination $\begin{pmatrix} \phi_1 \\ \phi_2 \end{pmatrix}$ defines a mode since the modal fields are then determined via (37), (34), (29), and the gradient of (27).

In general, there are two linearly independent choices for the vector $\begin{pmatrix} \phi_1 \\ \phi_2 \end{pmatrix}$, and these yield two linearly independent, charge distributions for the same TEM propagation constant, $\kappa = k$, i.e. there are two degenerate TEM modes. (This result also holds when more than one term is used in the strip-current expansion).

A convenient basis for the vector space $\{\begin{pmatrix} \phi_1 \\ \phi_2 \end{pmatrix}\}$, is one whose associated fields are orthogonal over the unit cell cross-section. It is shown in Appendix I that the eigenvectors of the capacitance matrix exhibit this property. The eigenvectors are

$$\phi_a = \begin{pmatrix} P_{12} \\ |P_{12}| \end{pmatrix}, \quad \phi_b = \begin{pmatrix} -P_{12} \\ |P_{12}| \end{pmatrix}. \quad (38)$$

They satisfy $\phi_a^T \cdot \phi_b = \delta_{a,b}$ where $\delta_{a,b}$ is the Kronecker delta function. The associated (real) eigenvalues are

$$\lambda_{a,b} = (P_{11} \mp |P_{12}|) / \Delta \quad , \quad (39)$$

where

$$\Delta = P_{11}^2 - |P_{12}|^2. \quad (40)$$

As seen from (38), for each eigenvector the component ratio, which represents the relative strip charge distribution for a given TEM mode, is of unit magnitude. Furthermore, the two modes have relative charge distributions which differ in phase by 180° .

IV. TM_2 MODES OF THE FEED REGION FOR A TRIANGULAR LATTICE

The analysis of Section II is now extended to the case of a triangular grid by choosing the unit cell shown in Figure 4. The Green's function (2) is also valid in this case. By imposing boundary conditions on all the strips a set of four integral equations is obtained, which are reduced to a set of linear, homogeneous algebraic equations via the Galerkin procedure. Imposing the steering phase shift between the two strip transmission lines, shown in Figure 4, reduces the problem to the solution of two equations in two unknowns, which in turn yields the dispersion relation and the modal current distribution.

In detail, the modal axial electric field generated by the strip current distribution, $J_i(y') \underline{z}_0$ ($i = 1, 2, 3, 4$), and with \hat{G} given in (2), is

$$E_z(\underline{r}; \kappa, \underline{k}_{t0}) = e^{-j\kappa z} \sum_{i=1}^4 \left[\int_{\text{strip } i} \hat{G}(\underline{\rho}, \underline{\rho}'; \kappa, \underline{k}_{t0}) J_i(y') dy' \right] \quad (41)$$

The integral equations are obtained by requiring E_z to vanish on each of the four conductors. In reducing these to algebraic equations one term is used in the current expansion, as previously in (14).

For the choice $\Psi(y') = 1$, the set of equations is

$$\begin{pmatrix} Z_{11} & Z_{12} & Z_{13} & Z_{14} \\ Z_{12}^* & Z_{11} & Z_{23} & Z_{13} \\ Z_{13}^* & Z_{23}^* & Z_{11} & Z_{12} \\ Z_{14}^* & Z_{13}^* & Z_{12}^* & Z_{11} \end{pmatrix} \begin{pmatrix} \alpha_1 \\ \alpha_2 \\ \alpha_3 \\ \alpha_4 \end{pmatrix} = 0 \quad (42)$$

where the independent coefficients of the Hermitian matrix are:

$$Z_{11}(\kappa, \underline{k}_{to}) = \sum_{n=-\infty}^{\infty} \frac{1}{k_{xn}} \cdot \frac{\sin(k_{xn} d_x)}{\cos k_{xn} d_x - \cos \xi d_x} \left(\frac{\sin \frac{k_{yn} h}{2}}{\frac{k_{yn} h}{2}} \right)^2 \quad (43)$$

$$Z_{12}(\kappa, \underline{k}_{to}) = \sum_{n=-\infty}^{\infty} \frac{1}{k_{xn}} \cdot \frac{\sin k_{xn} (d_x - w) e^{j\xi d_x} \sin k_{xn} w}{\cos k_{xn} d_x - \cos \xi d_x} \left(\frac{\sin \frac{k_{yn} h}{2}}{\frac{k_{yn} h}{2}} \right)^2 \quad (44)$$

$$Z_{13}(\kappa, \underline{k}_{to}) = \sum_{n=-\infty}^{\infty} \frac{2}{k_{xn}} \cdot \frac{e^{\frac{j\xi d_x}{2} \cos \frac{\xi d_x}{2}} \sin \frac{k_{xn} d_x}{2}}{\cos k_{xn} d_x - \cos \xi d_x} \left(\frac{\sin \frac{k_{yn} h}{2}}{\frac{k_{yn} h}{2}} \right)^2 e^{jk_{yn} d_y} \quad (45)$$

$$Z_{14}(\kappa, \underline{k}_{to}) = \sum_{n=-\infty}^{\infty} \frac{1}{k_{xn}} \cdot \frac{\sin k_{xn} (d_x/2 - w) e^{j\xi d_x} \sin k_{xn} (d_x/2 + w)}{\cos k_{xn} d_x - \cos \xi d_x} \left(\frac{\sin \frac{k_{yn} h}{2}}{\frac{k_{yn} h}{2}} \right)^2 e^{jk_{yn} d_y} \quad (46)$$

$$Z_{23}(\kappa, \underline{k}_{to}) = \sum_{n=-\infty}^{\infty} \frac{1}{k_{xn}} \cdot \frac{\sin k_{xn} (d_x/2 + w) e^{j\xi d_x} \sin k_{xn} (d_x/2 - w)}{\cos k_{xn} d_x - \cos \xi d_x} \left(\frac{\sin \frac{k_{yn} h}{2}}{\frac{k_{yn} h}{2}} \right)^2 e^{jk_{yn} d_y} \quad (47)$$

Imposition of the steering phase requirements between the two

feed lines, i.e., $\alpha_{i+2} = \alpha_i e^{-j(\xi d_x + \frac{\eta d_y}{2})}$, where ξ and η are defined in

(6-7), yields

$$\begin{pmatrix} \hat{Z}_1 & \hat{Z}_2 \\ \hat{Z}_3 & \hat{Z}_1 \\ \hat{Z}_1^* & \hat{Z}_3^* \\ \hat{Z}_2^* & \hat{Z}_1^* \end{pmatrix} \begin{pmatrix} \alpha_1 \\ \alpha_2 \end{pmatrix} = 0 \quad (48)$$

with

$$\hat{Z}_1(\kappa, \underline{k}_{to}) = Z_{11}(\kappa, \underline{k}_{to}) + Z_{13}(\kappa, \underline{k}_{to}) e^{-j \left(\xi d_x + \frac{\eta d_y}{2} \right)} \quad (49)$$

$$\hat{Z}_2(\kappa, \underline{k}_{to}) = Z_{12}(\kappa, \underline{k}_{to}) + Z_{14}(\kappa, \underline{k}_{to}) e^{-j \left(\xi d_x + \frac{\eta d_y}{2} \right)} \quad (50)$$

$$\hat{Z}_3(\kappa, \underline{k}_{to}) = Z_{12}^*(\kappa, \underline{k}_{to}) + Z_{23}(\kappa, \underline{k}_{to}) e^{-j \left(\xi d_x + \frac{\eta d_y}{2} \right)} \quad (51)$$

Using (43-47) and (49-51) one finds that

$$\hat{Z}_1(\kappa, \underline{k}_{to}) = \hat{Z}_1^*(\kappa, \underline{k}_{to}) \quad (52)$$

$$\hat{Z}_2(\kappa, \underline{k}_{to}) = \hat{Z}_3^*(\kappa, \underline{k}_{to}) \quad (53)$$

and (48) reduces to

$$\begin{pmatrix} \hat{Z}_1 & \hat{Z}_2 \\ \hat{Z}_2^* & \hat{Z}_1 \end{pmatrix} \begin{pmatrix} \alpha_1 \\ \alpha_2 \end{pmatrix} = 0 \quad (54)$$

yielding the dispersion relation for the triangular grid case

$$\hat{Z}_1^2(\kappa, \underline{k}_{to}) - |\hat{Z}_2(\kappa, \underline{k}_{to})|^2 = 0. \quad (55)$$

The TEM mode charge distributions for the triangular grid can be determined by a corresponding extension of the analysis presented in Section III.

Four inhomogeneous equations are obtained via Galerkin's procedure and, by imposing the steering phase requirements, are reduced to the form of (32), where

$$P_{11}(\underline{k}_{to}) = \frac{1}{2d_y \epsilon_0} \sum_{n=-\infty}^{\infty} \frac{1}{k_{yn}} \frac{\sinh k_{yn} d_x + 2 \cos(n\pi) \cos \frac{\xi d_x}{2} \sinh \frac{k_{yn} d_x}{2}}{\cosh k_{yn} d_x - \cos \xi d_x} \left(\frac{\sin \frac{k_{yn} h}{2}}{\frac{k_{yn} h}{2}} \right)^2 \quad (56)$$

$$\begin{aligned}
P_{12}(k_{to}) = & \frac{1}{2d_y \epsilon_0} \sum_{n=-\infty}^{\infty} \frac{1}{k_{yn}} \frac{\sinh k_{yn}(d_x - w) + e^{j\xi d_x} \sinh k_{yn} w}{\cosh k_{yn} d_x - \cos \xi d_x} \\
& + \frac{\cos(n\pi) e^{j\frac{\xi d_x}{2}} \sinh k_{yn}(\frac{d_x}{2} + w) + e^{-j\frac{\xi d_x}{2}} \sinh k_{yn}(\frac{d_x}{2} - w)}{\cosh k_{yn} d_x - \cos \xi d_x} \left(\frac{\sin \frac{k_{yn} h}{2}}{\frac{k_{yn} h}{2}} \right)^2
\end{aligned}$$

(57)

The charge distributions and fields may then be calculated as indicated in Section II.

V. NUMERICAL ANALYSIS

The TM propagation constants, which are the roots of (24), were evaluated by using a combination of the step searching method and the secant method. For small values of h/λ (Fig. 3), convergence of the series (21) was accelerated using the closed form expression [6] for $\sum_{n=1}^{\infty} \frac{\sin^2 n\alpha}{n^3}$. Series (22) converges well because its terms decay exponentially with n . The curves of Figs. 5-8, were obtained with n ranging from -20 to 20. Extending the range of n from -200 to 200 did not change the third significant digit of either (21), (22) or $\frac{k}{k}$.

In computing the curves shown in Figs. 5-8 a single constant term was used for the current expansion on each strip. Curves were also computed using the single static term (23) and a comparison of results for these two current choices is shown in Fig. 9.

For the scan plane $\phi = 90^\circ$, the unit cell of Fig. 3 can be bisected (Fig. 10). A magnetic wall is used because for the range of parameters over which $\frac{k}{k}$ was calculated, the currents on the two strips are in phase. This relationship is obtained by evaluating (21) and (22) (both are real for $\phi = 90^\circ$) and solving for $\alpha_{1,2}$ in (20). The bisected cell is identical to the unit cell of a one-dimensional strip grating bordered by magnetic walls. A circuit representation of the grating is used to construct an equivalent network [6], whose transverse resonance solution yields a dispersion relation for our bisected unit cell. The propagation constants obtained from this relation are in close agreement with those calculated from (24), except near cutoff.

The phase angle of the relative current distribution vs. scan is shown in Fig. 11 for the dominant, plus-minus, TEM mode. The phase angle for the plus-plus TEM mode is obtained from Fig. 11 by adding 180° to each phase value shown. The angles are measured using the left strip (Fig. 3) as the reference. The relative charge distributions were calculated using eigenvectors (38). Series (36) was evaluated with n ranging from -20 to 20.

Exactly at broadside the TEM plus-plus mode does not exist, since all the conductors are at the same potential.

For the triangular grid, the TM propagation constants (Fig. 12) and the TEM current distribution (Fig. 13) were calculated in similar fashion except that (21) was replaced by (49) and (22) by (50). The series of (43), contained in (49), is identical to that in (21) and its convergence can be accelerated as discussed above. The other series in (49) and (50) all converge rapidly.

The calculations for the rectangular and triangular grids were performed by computer programs which were checked against each other for the special case of the strip separation, w , equal to one-half the unit cell x -dimension, since in that case the two grids are identical.

VI. NUMERICAL RESULTS AND CONCLUSIONS

Figures (5-8 and 12) indicate that under appropriate conditions a propagating TM mode exists in the feed region of a dipole array. The normalized propagation constant of this mode for a rectangular grid geometry is shown in Fig. 5-8 for different values of d_x/λ , d_y/λ , w/λ and h/λ , respectively. It is seen that $\frac{k}{k_0}$ increases when the unit cell dimensions increase, or when the strip separation w/λ , or the strip width h/λ , decrease. Figures 5-8 show that $\frac{k}{k_0}$ decreases monotonically with azimuthal angle ϕ and elevation angle θ . However, in Fig. 6, $\frac{k}{k_0}$ decreases monotonically with elevation angle, only.

In Fig. 12, $\frac{k}{k_0}$ is shown vs. scan for two equilateral triangular grids. Here too, $\frac{k}{k_0}$ increases as the unit cell dimensions increase.

The TM strip currents are not shown in the figures. However, knowledge of the modal propagation constants makes it possible to evaluate the currents from (20). For each mode, (24) must be satisfied and $Z_{11} = \pm |Z_{12}|$. By substituting this result into (20) it is seen that the modal strip currents have the same magnitude and only differ in phase. This result holds for both the rectangular and the triangular array grids.

The relative TEM current distribution of the dominant, plus-minus, mode is shown in Figs. 11 and 13. It is seen that the maximum deviation of the current phase angle is about 12° . As stated previously, the distribution of the plus-plus mode, which is orthogonal to the plus-minus mode, is determined by adding 180° to the values shown in Figs. 11 and 13.

The most interesting feature observed in Figs. (5-8 and 12) is that the propagating TM mode may cut off with scan angle before the endfire grating lobe appears in real space. The possibility that this cutoff causes the dipole array blindness is being investigated.

APPENDIX: TEM MODE ORTHOGONALITY

It will be shown for the general case of multimode strip current expansions that the capacitance matrix in (37) is Hermitian, and that its eigenvectors represent strip potentials which generate two orthogonal TEM fields.

The potential in the unit cell of Fig. 3 is described by

$$\phi(x, y) = G(x, y, \frac{w}{2}, y'; k_{to})\eta_1(y') + G(x, y, \frac{w}{2}, y'; k_{to})\eta_2(y') \quad (A1)$$

where G is defined as in (25), $G\eta$ as in (13), and $\eta_{1,2}$ are the strip charge densities.

Imposing the boundary conditions on the conductors yields the integral equations for $\eta_{1,2}$

$$\begin{aligned} \phi_1 &= \phi(-\frac{w}{2}, y) \\ & , \quad \text{for } |y| \leq \frac{h}{2} \\ \phi_2 &= \phi(\frac{w}{2}, y), \end{aligned} \quad (A2)$$

where $\phi_{1,2}$ are the constant potential values on the strips.

In solving (A2), the charge densities $\eta_{1,2}$ are approximated by the finite series,

$$\begin{aligned} \eta_1(y') &= \sum_{p=1}^P \alpha_{1p} \psi_p(y') \\ \eta_2(y') &= \sum_{p=1}^P \alpha_{2p} \psi_p(y'), \end{aligned} \quad (A3)$$

where $\psi_p(y')$ are real, linearly independent, basis functions.

Substituting (A3) into (A2) and projecting both sides of (A2) on to the basis functions $\psi_p(y')$ results in a set of $2P \times 2P$, linear, inhomogeneous algebraic equations,

$$\begin{aligned} \langle \phi_1, \psi_q \rangle &= \langle \phi(-\frac{w}{2}, y), \psi_q \rangle \\ \langle \phi_2, \psi_q \rangle &= \langle \phi(\frac{w}{2}, y), \psi_q \rangle, \end{aligned} \quad (q = 1, 2, \dots, P) \quad (A4)$$

where $\langle f, g \rangle$ is defined in (17).

Equations (A4) can be written in the partitioned matrix form,

$$\underline{\phi} = \underline{M} \underline{\alpha}, \quad (A5)$$

where

$$\underline{M} = \begin{pmatrix} \underline{A} & | & \underline{B} \\ \hline \underline{B}^+ & | & \underline{A} \end{pmatrix} \quad (A6)$$

is Hermitian due to symmetries

$$G(x', y, x', y') = G^*(-x', y', -x', y) \quad (A7)$$

and

$$G(x, y, x', y') = G^*(x', y', x, y). \quad (A8)$$

The elements of the submatrices \underline{A} and \underline{B} , in (A6), are

$$a_{qp} = \langle \psi_q(y), G(-\frac{w}{2}, y, -\frac{w}{2}, y') \psi_p(y') \rangle \quad (A9)$$

$$b_{qp} = \langle \psi_q(y), G(-\frac{w}{2}, y, \frac{w}{2}, y') \psi_p(y') \rangle, \quad (A10)$$

and the vectors $\underline{\alpha}$ and $\underline{\phi}$ are defined by

$$\underline{\alpha} = (\alpha_{11}, \dots, \alpha_{1P}, \alpha_{21}, \dots, \alpha_{2P})^T \quad (A11)$$

and

$$\underline{\phi} = (\phi_1 \langle 1, \psi_1 \rangle, \dots, \phi_1 \langle 1, \psi_p \rangle, \phi_2 \langle 1, \psi_1 \rangle, \dots, \phi_2 \langle 1, \psi_p \rangle)^T. \quad (\text{A12})$$

Assuming that \underline{M} is non-singular,

$$\underline{\alpha} = \underline{M}^{-1} \underline{\phi}, \quad (\text{A13})$$

where

$$\underline{M}^{-1} = \begin{pmatrix} \hat{\underline{A}} & | & \hat{\underline{B}} \\ \hat{\underline{B}}^+ & | & \hat{\underline{A}} \end{pmatrix} \quad (\text{A14})$$

is also Hermitian. By using the partitions of \underline{M}^{-1} , (A13) can be split into

$$\begin{aligned} \underline{\alpha}_1 &= \phi_1 \hat{\underline{A}} \underline{\gamma} + \phi_2 \hat{\underline{B}} \underline{\gamma} \\ \underline{\alpha}_2 &= \phi_1 \hat{\underline{B}}^+ \underline{\gamma} + \phi_2 \hat{\underline{A}} \underline{\gamma} \end{aligned} \quad (\text{A15})$$

where

$$\underline{\alpha}_i = (\alpha_{i1}, \dots, \alpha_{ip})^T \quad (i = 1, 2) \quad (\text{A16})$$

and

$$\underline{\gamma} = (\langle 1, \psi_1 \rangle, \dots, \langle 1, \psi_p \rangle)^T. \quad (\text{A17})$$

The charge on the strips per unit length in z is

$$Q_i = \sum_{p=1}^P \alpha_{ip} \langle 1, \psi_p \rangle = \underline{\gamma}^T \underline{\alpha}_i \quad (i = 1, 2). \quad (\text{A18})$$

Then premultiplying (A13) with $\underline{\gamma}^T$ yields

$$\begin{aligned} Q_1 &= \phi_2 (\underline{\gamma}^T \hat{\underline{A}} \underline{\gamma}) + \phi_2 (\underline{\gamma}^T \hat{\underline{B}} \underline{\gamma}) \\ Q_2 &= \phi_1 (\underline{\gamma}^T \hat{\underline{B}}^+ \underline{\gamma}) + \phi_2 (\underline{\gamma}^T \hat{\underline{A}} \underline{\gamma}). \end{aligned} \quad (\text{A19})$$

which can be written in the matrix form,

$$\begin{pmatrix} Q_1 \\ Q_2 \end{pmatrix} = \underline{C} \begin{pmatrix} \phi_1 \\ \phi_2 \end{pmatrix} \quad (\text{A20})$$

where the capacitance matrix, \underline{C} , is Hermitian because $\underline{\gamma}$ is real. Therefore, the eigenvalues of the matrix are real and the corresponding eigenvectors are mutually orthogonal. In general, (A20) has two linearly independent solutions, which implies that two linearly independent TEM modes exist in the unit cell of Fig. 3.

It will now be shown that when the strip potentials are chosen equal to the eigenvectors of \underline{C} their associated TEM field distributions are orthogonal over the unit cell.

Let $\lambda_{a,b}$ be the two eigenvalues of \underline{C} , let $\begin{pmatrix} \phi_{a1} \\ \phi_{a2} \end{pmatrix}$ and $\begin{pmatrix} \phi_{b1} \\ \phi_{b2} \end{pmatrix}$ be the associated eigenvectors, let $\phi_{a,b}(x,y)$ be the corresponding electrostatic potentials in the unit cell, and let

$$I = \iint_{\text{unit cell}} \nabla \phi_a(x,y) \cdot \nabla \phi_b^*(x,y) dx dy. \quad (\text{A21})$$

It is desired to show that $I = 0$. The surface integral of (A21) can be converted, via Green's Theorem, into the line integral

$$I = \oint_C \phi_a(x,y) \frac{\partial \phi_b^*(x,y)}{\partial n} dx, \quad (\text{A22})$$

where the integration path C runs counterclockwise over the unit cell boundary and clockwise over a closed contour hugging the strips. By Floquet's Theorem, the contributions to the integral from opposite sides of the unit cell boundary cancel. Therefore, (A22) equals the contribution from the strips, that is

$$\begin{aligned} I &= \int_{-\frac{h}{2}}^{\frac{h}{2}} \phi_a\left(-\frac{w}{2}, y\right) \left[\frac{\partial \phi_b^*\left(-\frac{w}{2}, y\right)}{\partial x} - \frac{\partial \phi_b^*\left(-\frac{w}{2}, y\right)}{\partial x} \right] dy \\ &+ \int_{-\frac{h}{2}}^{\frac{h}{2}} \phi_a\left(\frac{w}{2}, y\right) \left[\frac{\partial \phi_b^*\left(\frac{w}{2}, y\right)}{\partial x} - \frac{\partial \phi_b^*\left(\frac{w}{2}, y\right)}{\partial x} \right] dy \end{aligned} \quad (\text{A23})$$

(the normal points toward the strips). The terms in the brackets represent a discontinuity in the normal electric field across the strips. This discontinuity is proportional to the strip charge density. Therefore,

$$I = \frac{1}{\epsilon_0} \langle \phi_a(-\frac{w}{2}, y), \eta_{b1}^* \rangle + \frac{1}{\epsilon_0} \langle \phi_a(\frac{w}{2}, y), \eta_{b2}^* \rangle, \quad (A24)$$

where η_{b1} and η_{b2} are the respective, strip charge densities associated with eigenvector $\begin{pmatrix} \phi_{b1} \\ \phi_{b2} \end{pmatrix}$. By expanding η_b according to (A3), one finds that

$$I = \frac{1}{\epsilon_0} \sum_{p=1}^P \alpha_{b1p}^* \langle \phi_a(-\frac{w}{2}, y), \psi_p \rangle + \frac{1}{\epsilon_0} \sum_{p=1}^P \alpha_{b2p}^* \langle \phi_a(\frac{w}{2}, y), \psi_p \rangle, \quad (A25)$$

and, therefore, from (A4)

$$I = \frac{\phi_{a1}}{\epsilon_0} \sum_{p=1}^P \alpha_{b1p}^* \langle 1, \psi_p \rangle + \frac{\phi_{a2}}{\epsilon_0} \sum_{p=1}^P \alpha_{b2p}^* \langle 1, \psi_p \rangle. \quad (A26)$$

Substituting from (A18),

$$I = \frac{\phi_{a1} \underline{Q}_{b1}^*}{\epsilon_0} + \frac{\phi_{a2} \underline{Q}_{b2}^*}{\epsilon_0}, \quad (A27)$$

which, from our previous definition of the eigenvalues and eigenvectors of \underline{Q} , can be written

$$I = \frac{\phi_{a1} \lambda_b \phi_{b1}^*}{\epsilon_0} + \frac{\phi_{a2} \lambda_b \phi_{b2}^*}{\epsilon_0} \quad (A28)$$

However,

$$\phi_{a1} \phi_{b1}^* + \phi_{a2} \phi_{b2}^* = 0$$

since the eigenvectors of \underline{Q} are orthogonal and consequently $I = 0$.

REFERENCES

1. J. D. Reale, "PAR Hardened Crossed-Dipole Array," 1974 Annual Tri-Service Radar Symposium Digest, pp. 351-364.
2. J. C. Herper, F. J. Esposito, C. Rothenberg and A. Hessel, "Surface Resonances in a Radome Covered Dipole Array," 1977 IEEE AP International Symposium Digest, pp. 198-201.
3. V. W. H. Chang, "Infinite Phased Dipole Array," IEEE Proceedings, Vol. 56, pp. 1892-1900, November 1968.
4. J. A. Fuller and R. L. Moore, "Hardened Phased Array Feasibility Assessment," Technical Report, Contract No. DASG60-76-C-0070, Georgia Inst. of Tech., Project A-1863, July 1977.
5. H. Steyskal, "On the Orthogonality of Approximate Waveguide Mode Functions," 1979 IEEE AP International Symposium Digest, pp. 433-436.
6. N. Marcuvitz, Waveguide Handbook, New York: Dover, 1965, p. 284.

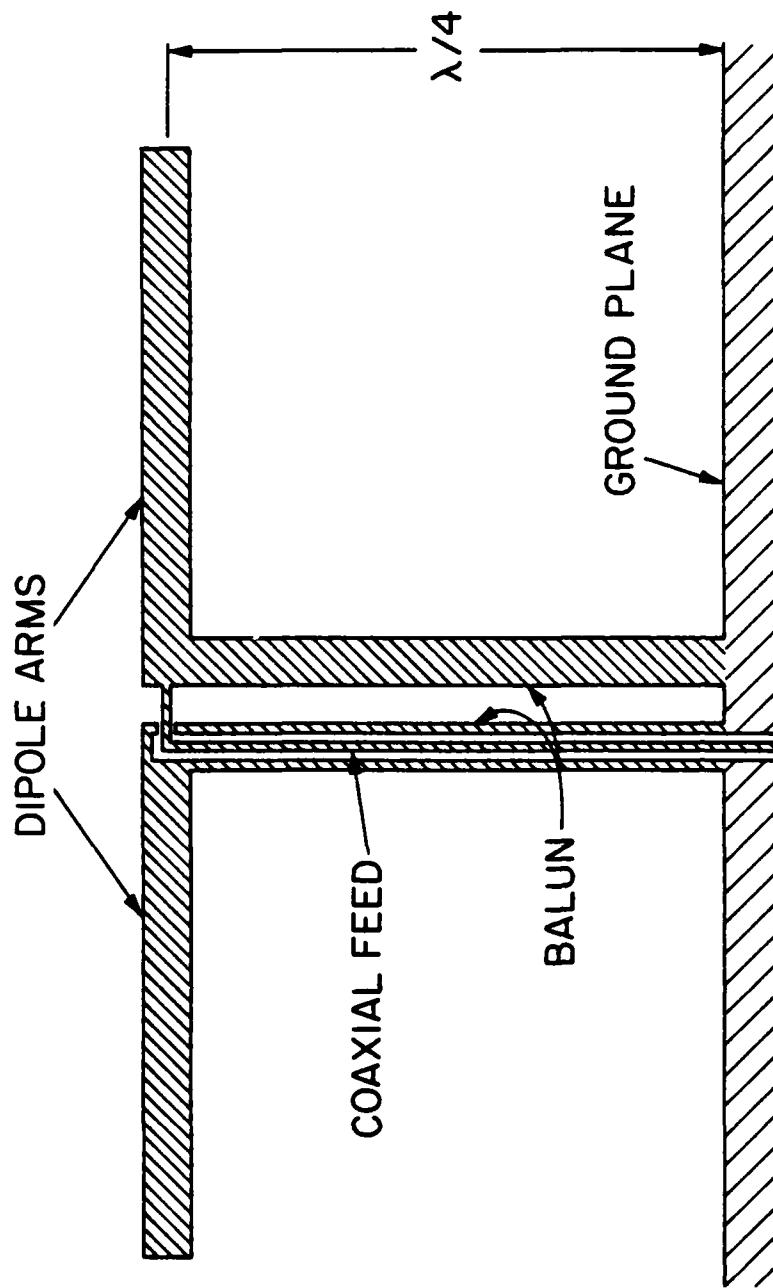


Fig. 1 Dipole array element with its balun feed structure.

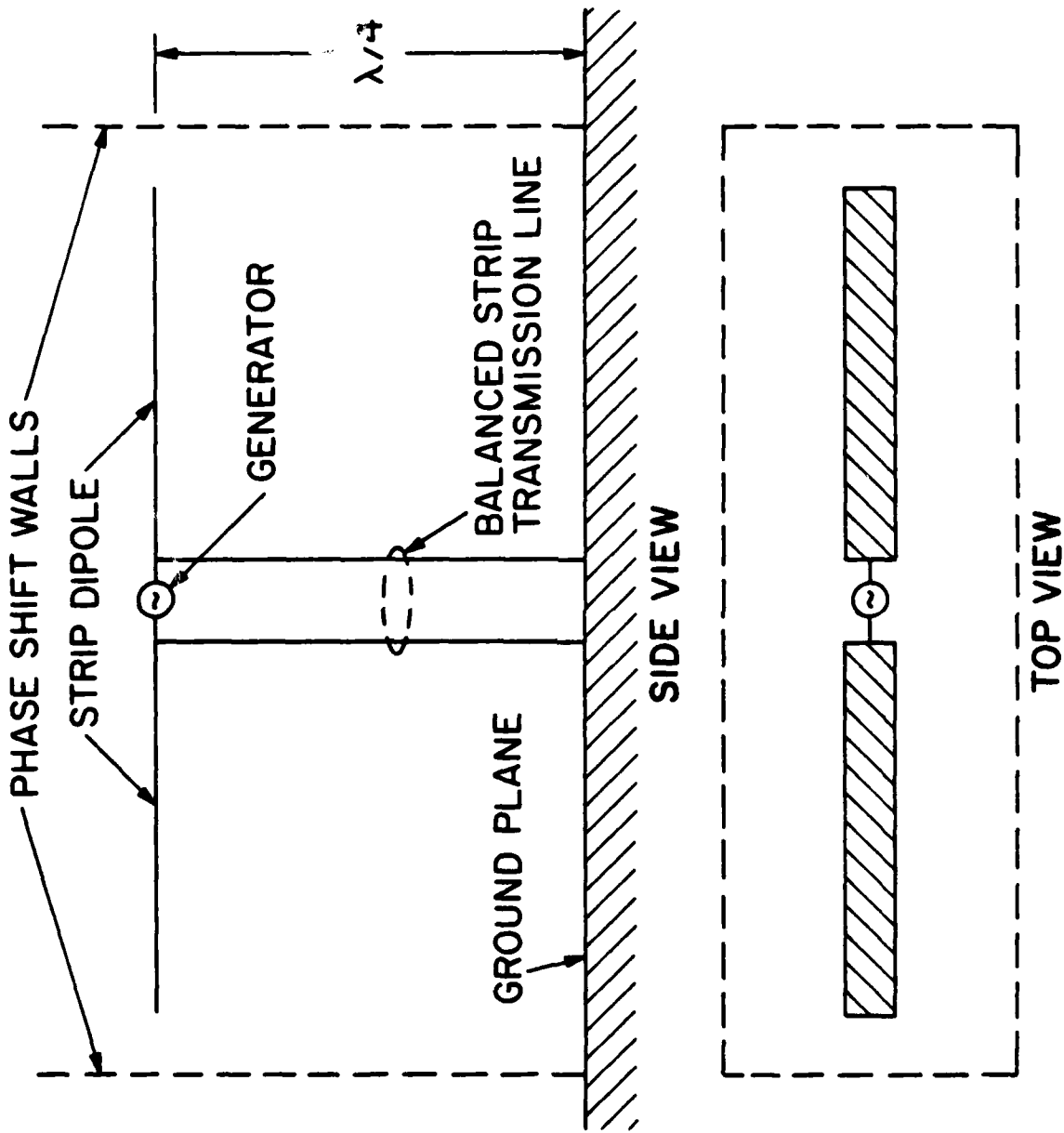


Fig. 2 Strip-line model of dipole array element.

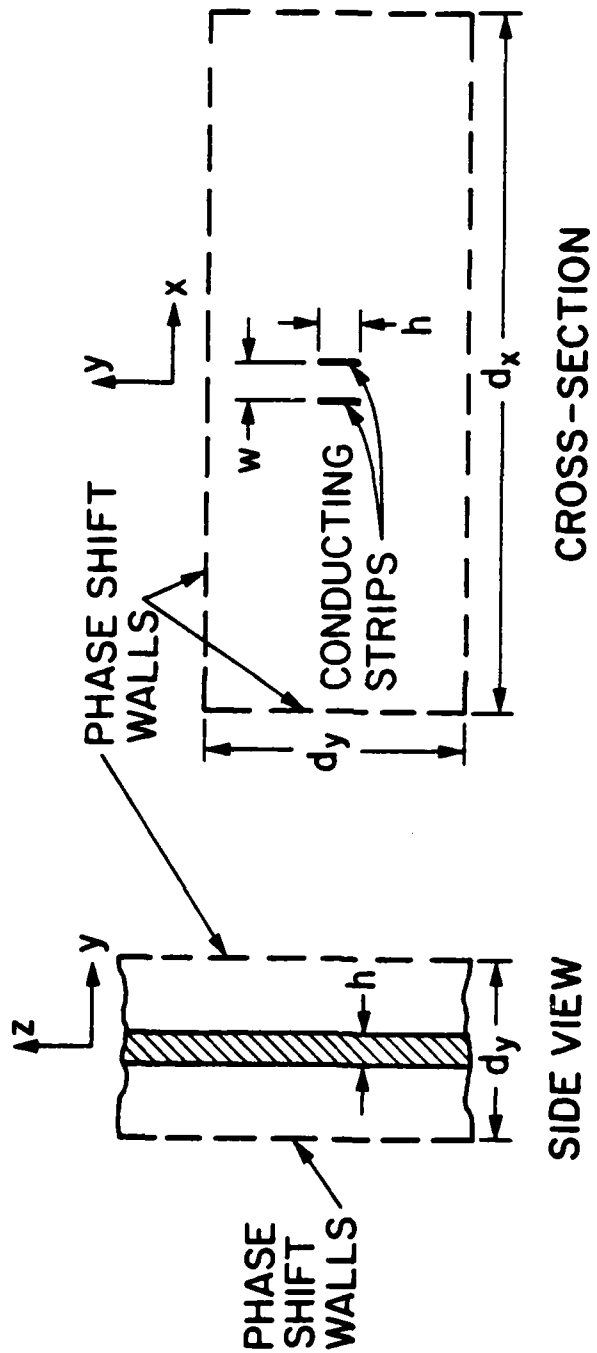
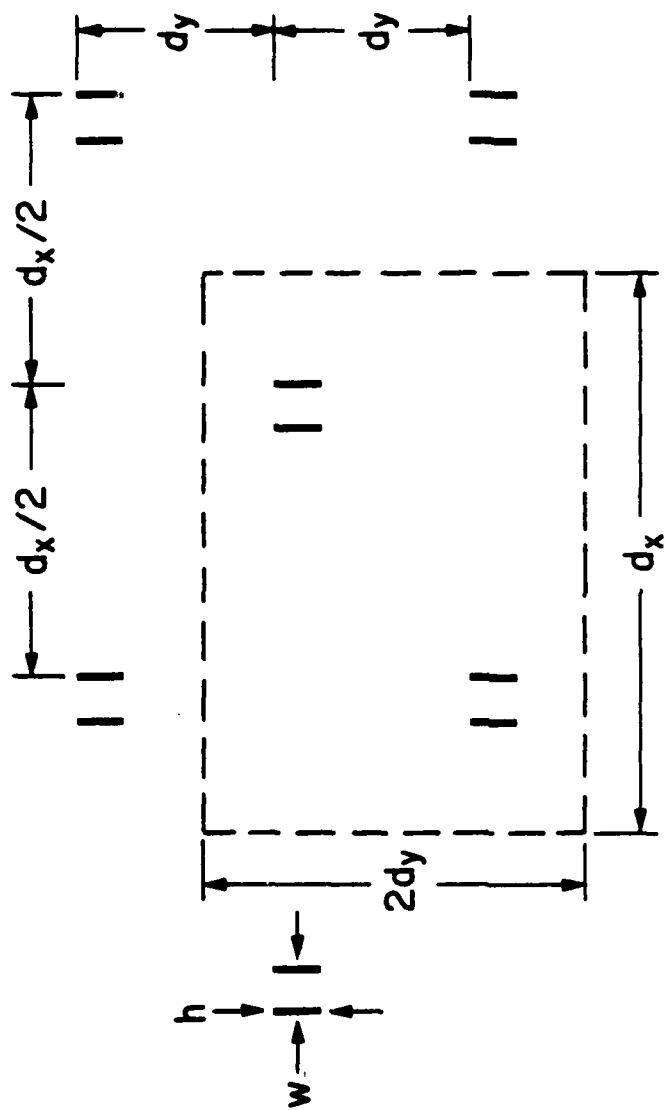


Fig. 3 Rectangular-grid unit-cell waveguide with balanced strip-transmission-line loading.



**CROSS-SECTION OF UNIT CELL
FOR TRIANGULAR GRID**

Fig. 4 Modified rectangular unit-cell for the analysis of feed region modes in triangular-grid arrays.

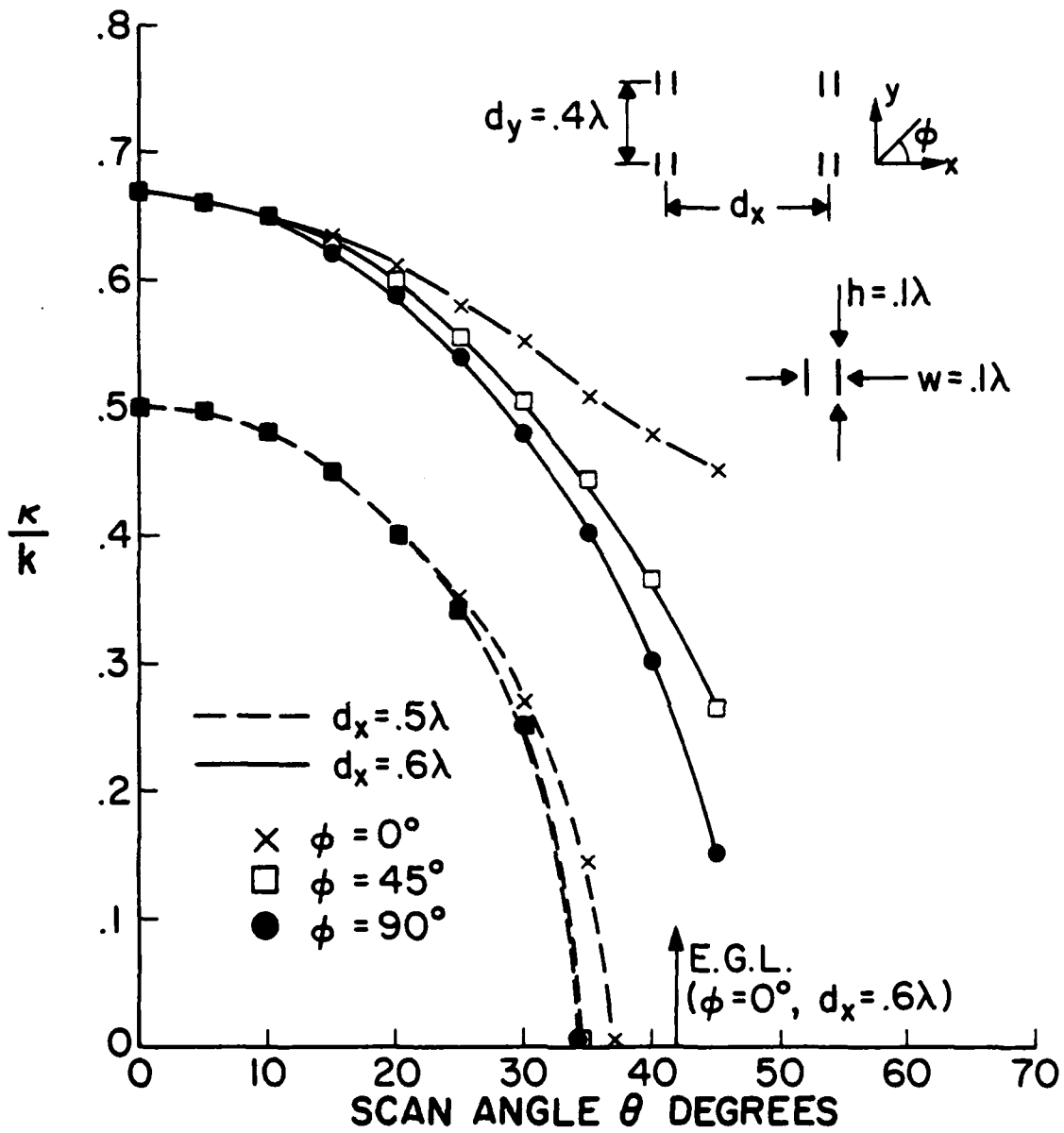


Fig. 5 Phase constant of the propagating TM_z mode vs. scan angle for the loaded unit-cell waveguide of Fig. 3, showing its dependence on d_x (E-plane spacing).

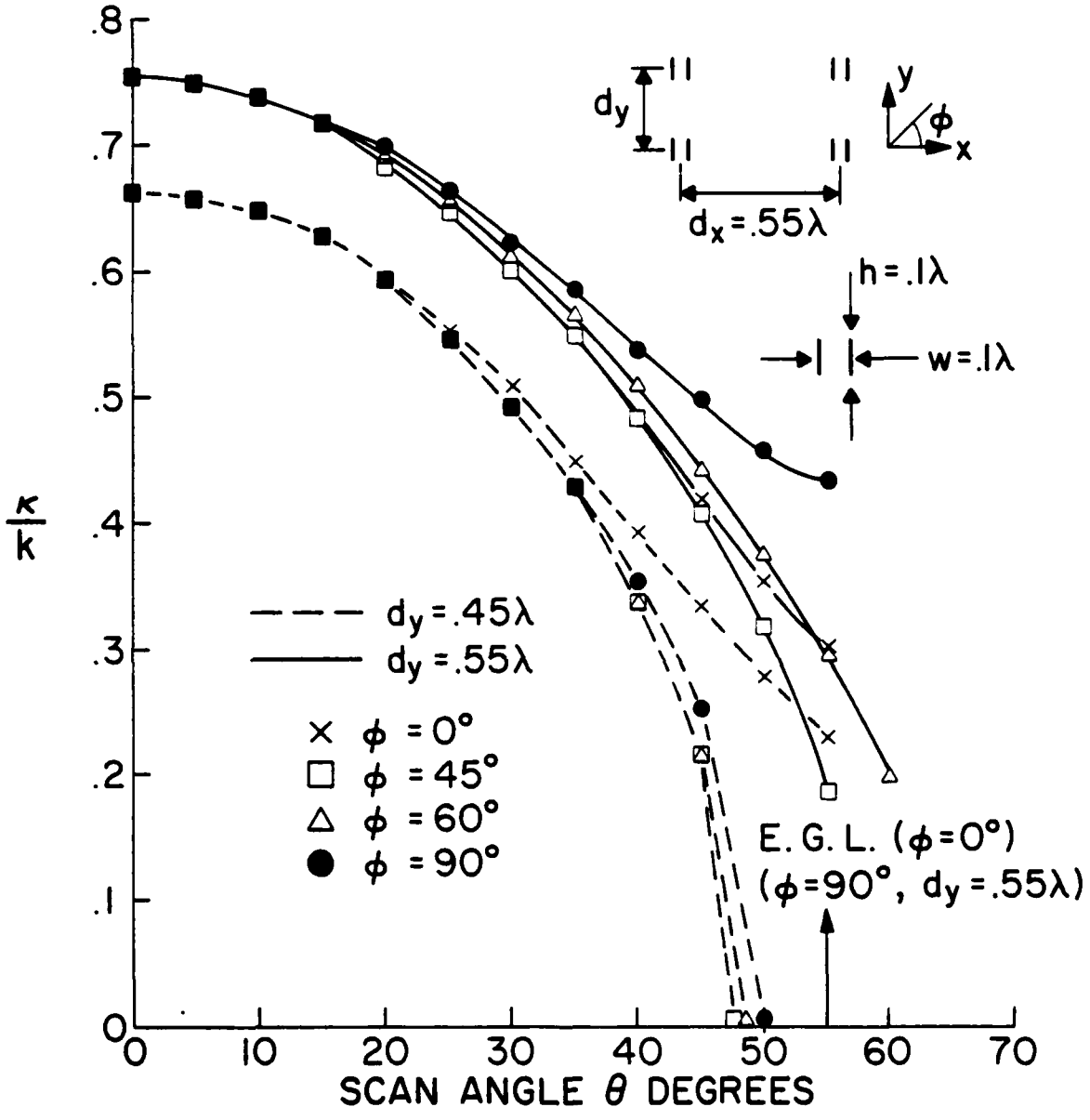


Fig. 6 Phase constant of the propagating TM_z mode vs. scan angle for the loaded unit-cell waveguide of Fig. 3, showing its dependence on d_y (H-plane spacing).

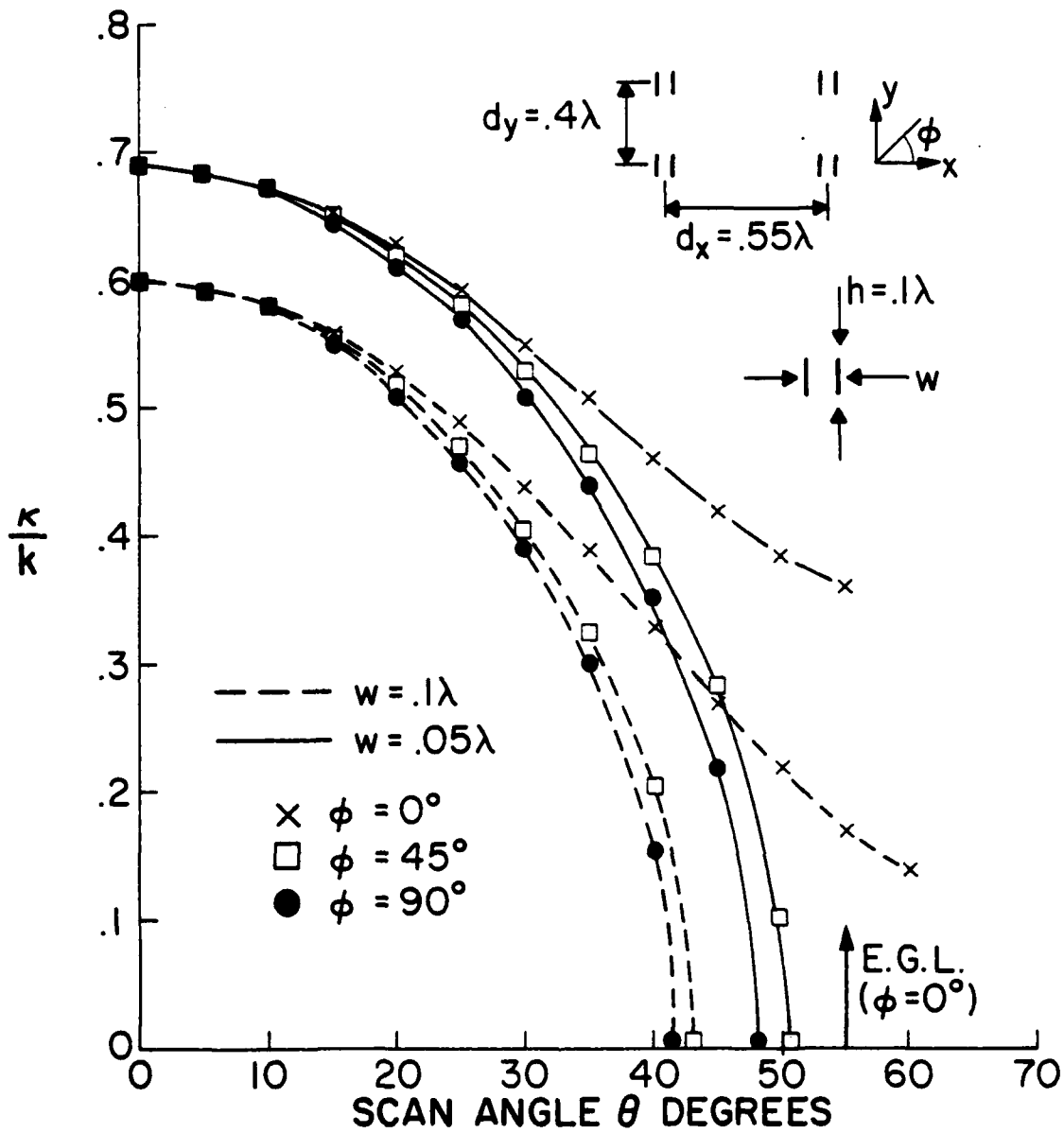


Fig. 7 Phase constant of the propagating TM_z mode vs. scan angle for the loaded unit-cell waveguide of Fig. 3, showing its dependence on w (strip separation).

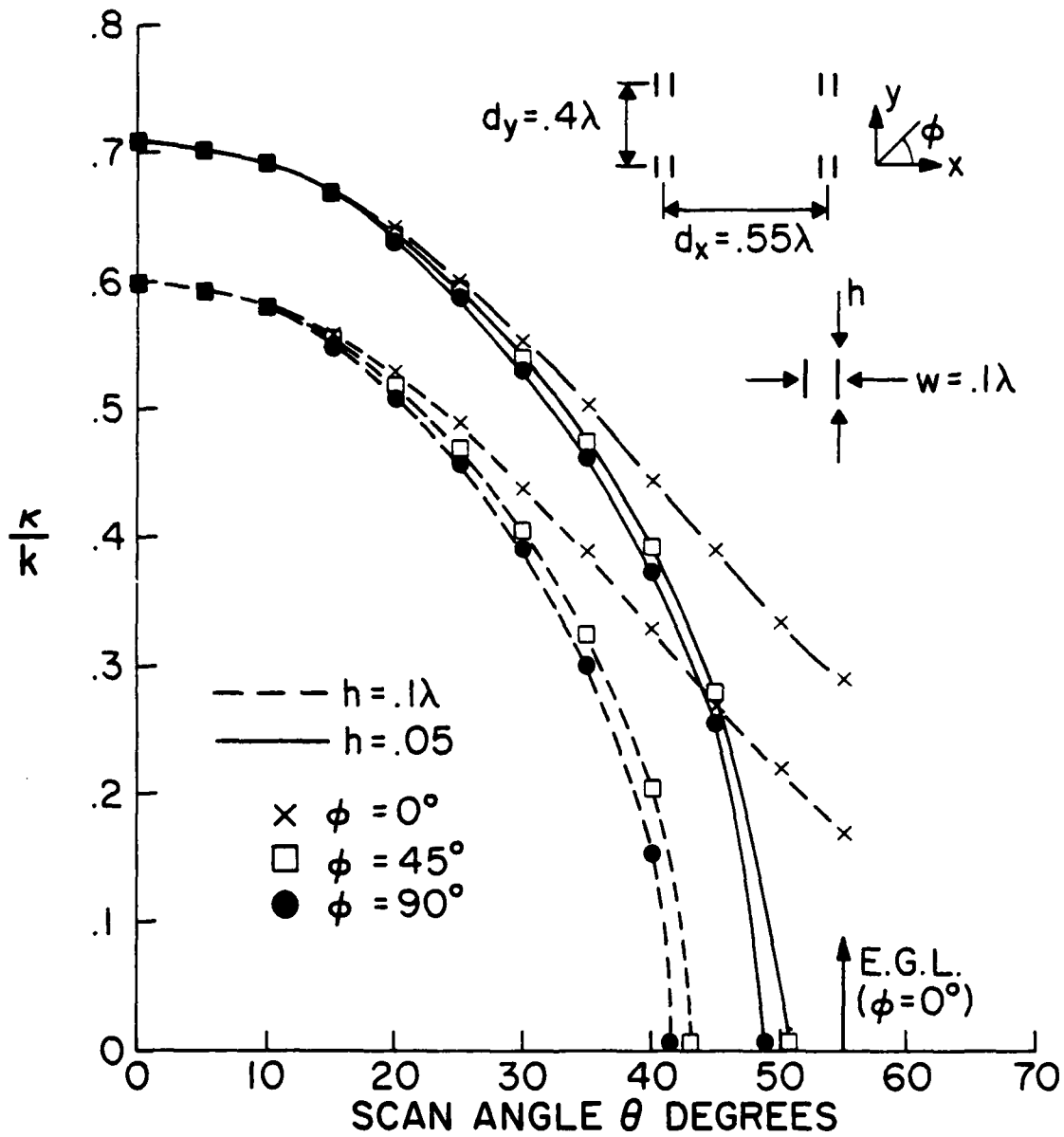


Fig. 8 Phase constant of the propagating TM_z mode vs. scan angle for the loaded unit-cell waveguide of Fig. 3, showing its dependence on h (strip width).

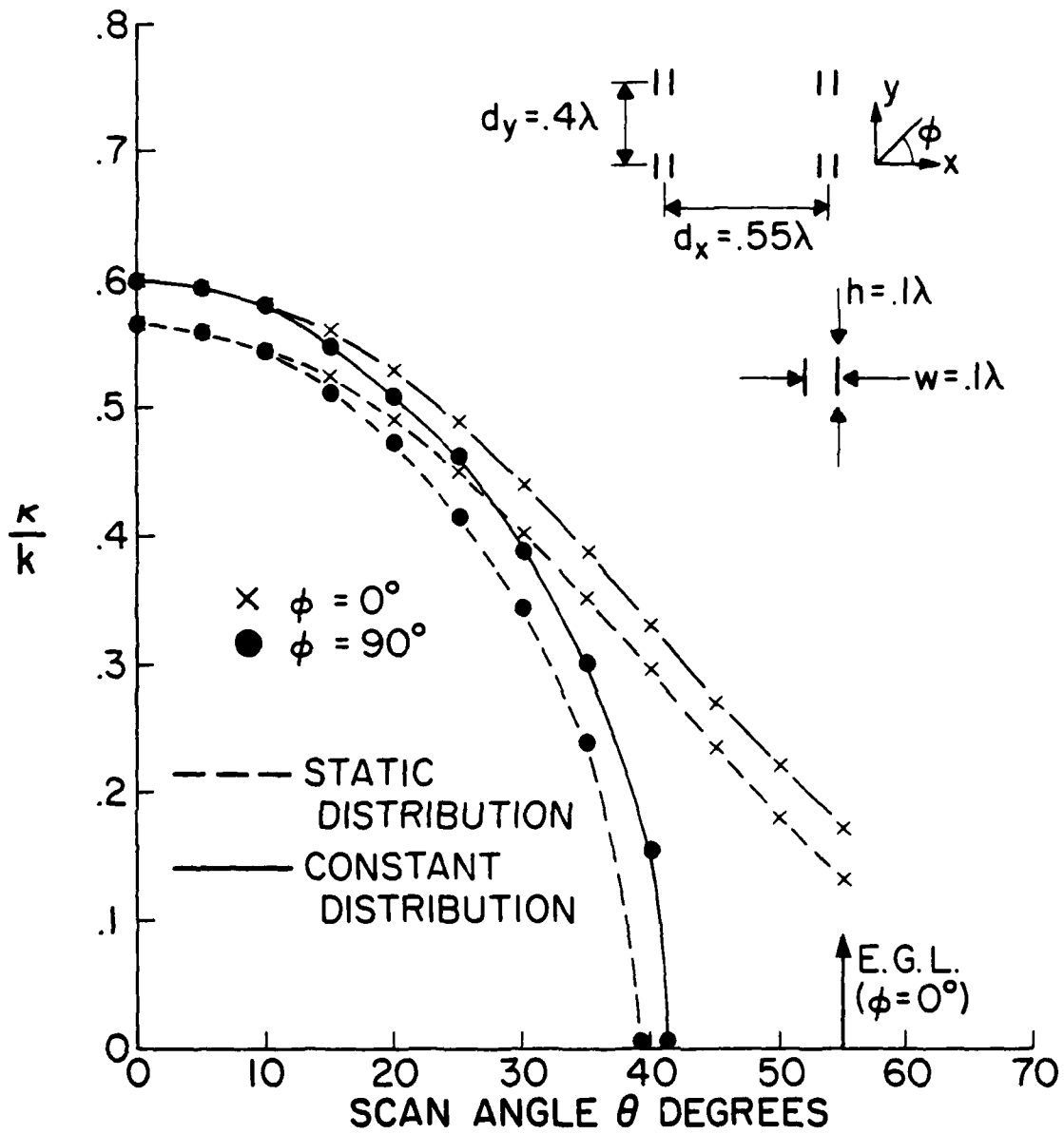


Fig. 9 Phase constant of the propagating TM_z mode vs. scan angle for the loaded unit-cell waveguide of Fig. 3, showing its dependence on the strip current distribution.

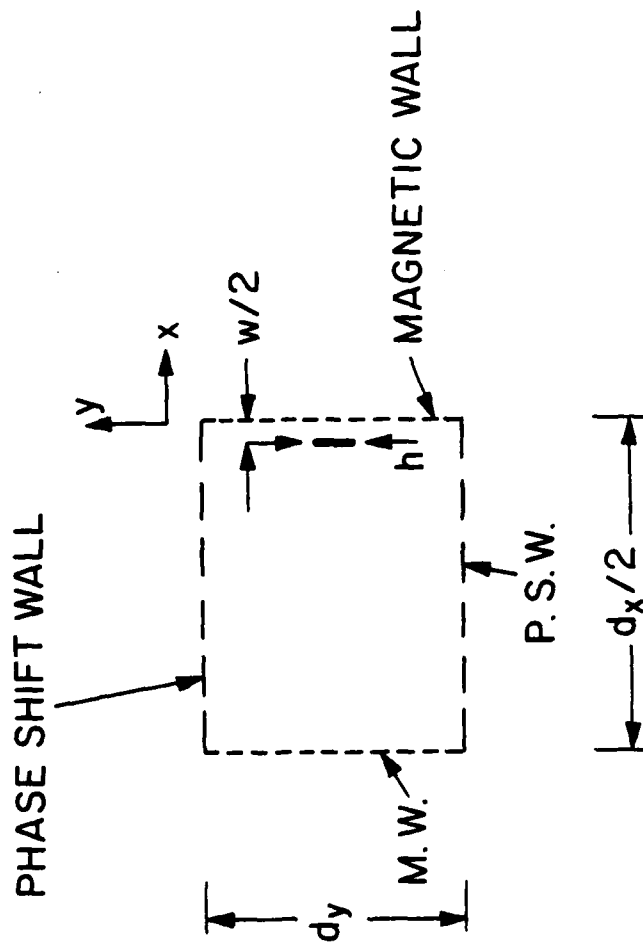


Fig. 10 Bisection of the unit cell of Fig. 3, for H-plane scan.

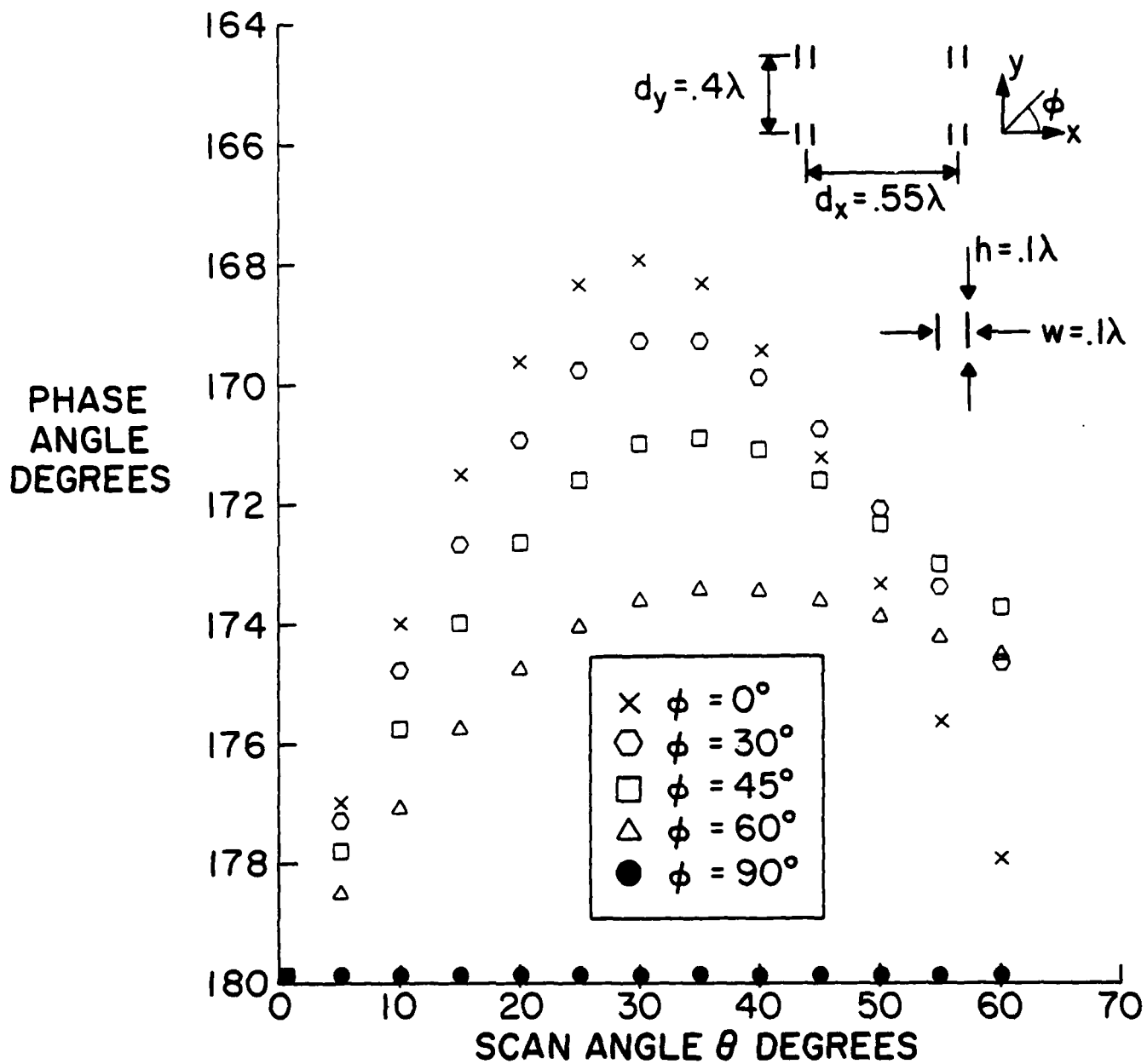


Fig. 11 Phase difference of the plus-minus TEM strip currents vs. scan angle for the loaded unit-cell waveguide of Fig. 3.

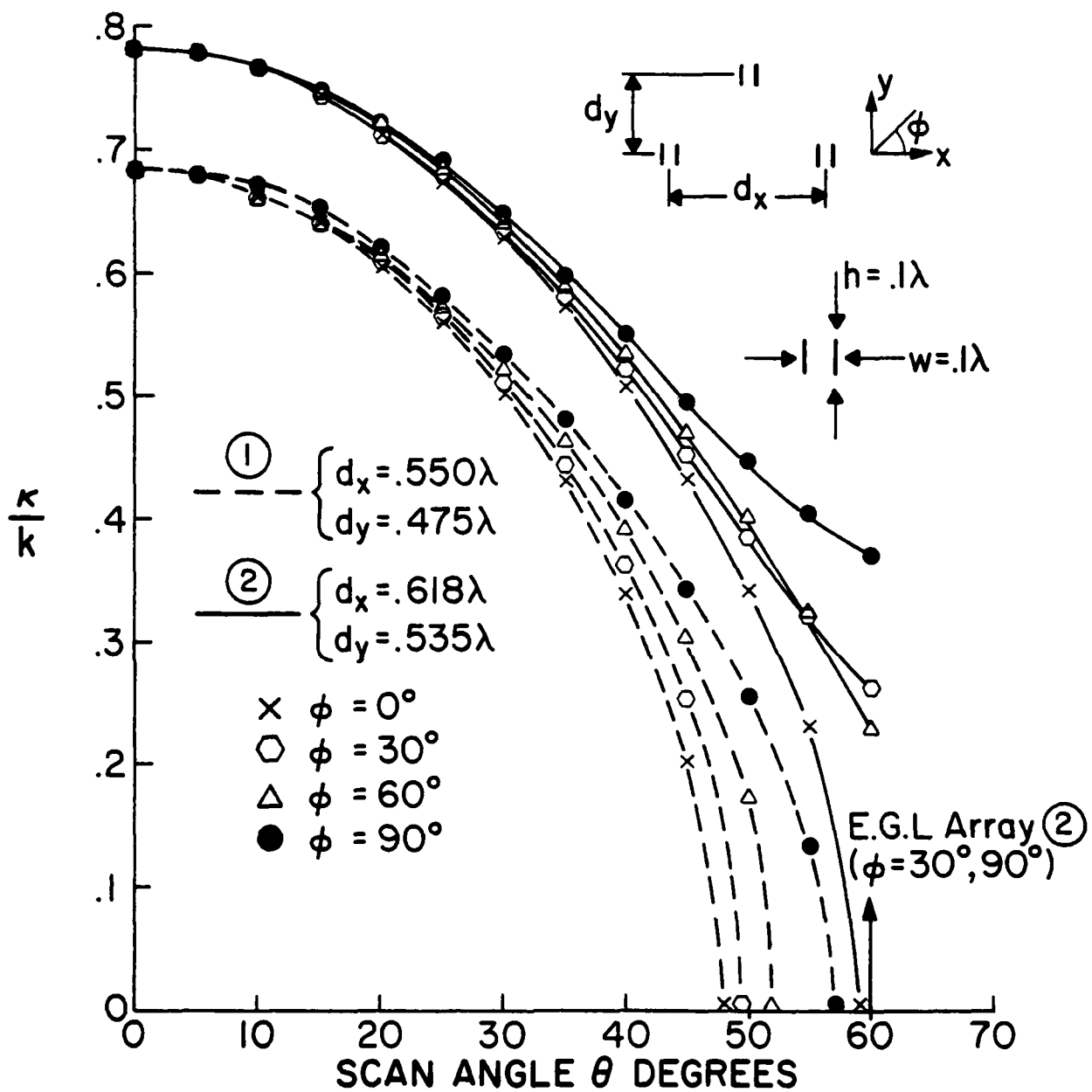


Fig. 12 Phase constant of the propagating TM_z mode vs. scan angle for the loaded unit-cell waveguide of Fig. 4. (triangular grid)

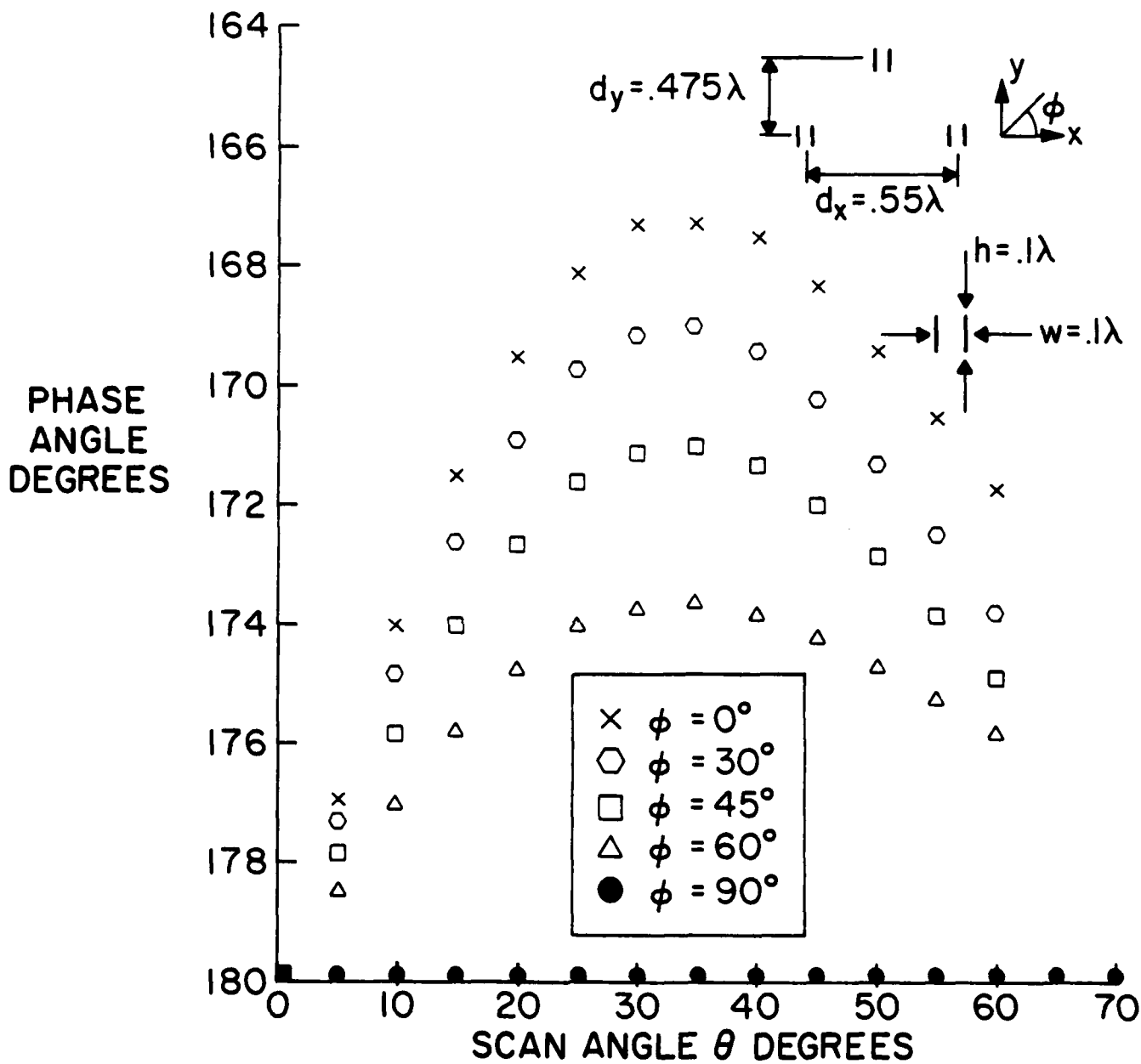


Fig. 13 Phase difference of the plus-minus TEM strip currents vs. scan angle for the loaded unit-cell waveguide of Fig. 4.

DATE
ILMED
-8